



Relationship Between Functional Fatigue and Structural Fatigue of Iron-Based Shape Memory Alloy FeMnNiAl

R. Sidharth¹ · Y. Wu¹ · F. Brenne¹ · W. Abuzaid² · H. Sehitoglu¹

Published online: 21 May 2020
© ASM International 2020

Abstract Utilizing FeMnNiAl single crystals subjected to fatigue loading, we make the important observation that the crack nucleation from the notch and the ensuing crack trajectory follows the most favorable martensite variants. These variants form in an asymmetric pattern with respect to the crack plane because of the underlying elastic anisotropy which is accounted for in the driving force analysis of the fatigue cracks. When the recoverable strain on a particular variant is exhausted, new variants are activated; this in turn changes the crack path. The activation of new variants also results in transient deceleration of the fatigue crack growth rates and upon subsequent growth, fatigue crack growth trends merge with the steady state behavior. Two surface analysis using FIB/TEM facilitated the unambiguous identification of the specific martensite variants responsible for fatigue crack growth. Displacement fields obtained via digital image correlation allowed for the determination of the local stress intensity which is inevitably affected by the activation/arrest of martensite variants. Hence, we make a direct link between the complex functional fatigue behavior and the fatigue crack growth behavior. Overall, the results show the steps to be considered to develop a framework for understanding fatigue crack growth response of shape memory alloys.

Keywords Superelasticity · Fatigue crack growth · Shape memory · Functional fatigue · Martensite

Introduction

The utilization of NiTi based shape memory alloys (SMA) in large-scale structural applications has been rather limited due to the high cost associated with this alloy system [1–3]. Iron-based SMA have the potential to address this limitation by offering a cost-effective alternative to NiTi. Among the Fe-based SMA compositions, Fe–Mn–Si [4, 5], Fe–Ni–Co–Al–Ti [6], Fe–Ni–Co–Ti [7–10], Fe–Pd [11], and more recently Fe–Mn–Ni–Al [9, 12–16] display promising attributes. The Fe–Mn–Ni–Al is of particular interest due to favorable mechanical and superelastic properties. High levels of superelastic strains (> 10%) at room temperature, with transformation stress levels in the range 400–600 MPa, have been reported for this SMA. With such high transformation stresses and strains, FeMnNiAl provides large work outputs that are very desirable for structural applications. In addition, FeMnNiAl exhibits a remarkable superelasticity window extending from – 196 to 300 °C which far exceeds NiTi (less than 100 °C). An extremely low Clausius–Clapeyron (CC) slope in FeMnNiAl, ($\partial\sigma_{tr}/\partial T$) of 0.5 MPa/°C in tension and 0.2 MPa/°C in compression [17], can also permit applications over a wide temperature interval. These unique properties of FeMnNiAl shape memory alloy renders it as a very attractive choice for structural applications. A comprehensive review of the FeMnNiAl system is provided in [18]. Despite extensive efforts, further work is required to better understand the properties of FeMnNiAl under fatigue loading conditions. The main focus of this work is on the fatigue crack growth behavior of FeMnNiAl. In particular,

✉ R. Sidharth
ravi8@illinois.edu

¹ Department of Mechanical Science and Engineering,
University of Illinois at Urbana-Champaign, 1206 W. Green
St., Urbana, IL 61801, USA

² Department of Mechanical Engineering, American
University of Sharjah, PO Box 26666, Sharjah, United Arab
Emirates

we study the role of transformation strain fields upon successive activation of variants, the modification of the crack tip driving forces, and evaluate the effective stress intensity levels responsible for crack advance.

Superelasticity, shape memory properties and reversibility of the martensitic transformation are heavily dependent on the SMA microstructural characteristics [17, 19–21]. Recent efforts have been primarily focused on the effect of grain size [22], grain orientation [22], heat treatment, aging and the resulting precipitates [19] on the superelastic and shape memory properties of FeMnNiAl. In general, achieving superelasticity requires a coarse microstructure and an optimized precipitate size and volume fraction. Small grains lead to early failure induced by grain boundary cracking and are detrimental to the alloy performance. In contrast, coarse microstructures having extremely large bamboo-type grains overcome these shortcomings and promote reversible thermoelastic transformation and large superelastic strains. The desirable microstructure has been typically realized through a cyclic heat treatment which induces abnormal grain growth [23]. However, for high levels of SE strains, proper control of the cooling process is additionally required to retain the single austenite bcc phase and prevent GB cracking during rapid cooling [19]. A final low temperature aging treatment is then conducted to facilitate the formation of nano-sized precipitates. This process promotes thermoelastic martensitic transformation by partially ordering the alloy system via the introduction of ordered NiAl precipitates in a disordered BCC austenite matrix and consequently amplifying the critical resolved shear stress (CRSS) for slip in the austenite matrix [9, 12, 24].

Iron-based SMAs, though very attractive in terms of cost and workability, seemingly show poor functional fatigue performance in comparison to NiTi. This is due to the irreversibility of the transformation resulting from extensive plastic deformation at the austenite–martensite interface [25–27]. Consequently, the accumulation of residual and irrecoverable strains at the expense of SE strains is typically observed. In fatigue crack growth, since extensive plastic deformation at the austenite–martensite interface [25–27] produces irreversibility, this mechanism could lower fatigue crack resistance based on our knowledge of fatigue crack growth research [28–30]. Thus, if the functional fatigue properties of this Fe-based SMA are limiting this could negatively impact the fatigue crack growth response. On the other hand, if activation of new variants partially restores superelasticity once the initial variants are exhausted, this mechanism could produce favorable fatigue crack growth (FCG) resistance. Such a study is missing to our knowledge.

Studies dedicated to investigating the fatigue crack growth properties of SMAs dates back to Melton and

Mercier [31] and Ritchie [32] on NiTi and recently by Sehitoglu et al. on NiTi [33, 34], Ni₂FeGa [35], and Cu–Zn–Al [36]. These works showed that fatigue crack growth resistance of SMAs are affected by multitude of factors including the transformation strains, elastic anisotropy, the test temperature, and the presence of stable austenite versus stable martensite or transforming austenite phases [37]. The derivation of driving forces during martensitic transformation deviating from standard handbook fracture mechanics solutions [35, 36, 38] should also be established in any study focused on FCG of SMAs. The notion of internal driving forces (including effective Mode II components) was introduced in our earlier work due to asymmetric transformation zones [36]. To facilitate such a description, one must confirm the activation of specific martensite variants at microscales. These issues are all described in detail in the present work.

In summary, our aim in this study is to underscore the difference between intrinsic crack growth resistance (e.g., failure due to cyclic irreversibility resulting in a net crack displacement per cycle) and the extrinsic response (affected by martensite-induced variables creating internal forces) and establish the threshold stress intensity factor and the critical stress intensity factor at fracture. The study aims to develop a methodology to explain the factors that govern the SMA FCG response.

Materials and Methods

Dog bone samples with 2 mm width, 1.5 mm thickness and 8 mm gauge length were cut out of a cast FeMn₃₄Ni_{7.5}Al₁₅ (at%) ingot using electro discharge machining (EDM). Each polycrystalline sample was individually encapsulated in quartz tube with low pressure argon atmosphere (< 50 mTorr) and subsequently subjected to a cyclic heat treatment (CHT) to induce abnormal grain growth (AGG) [23]. In this work, CHT was carried out between 800 and 1225 °C with a 30 min hold time at each temperature extreme as shown in Fig. 1. This cyclic treatment was repeated for four cycles and terminated with a 30 min hold at 1225 °C before quenching the sample in 80 °C warm water. Quenching in warm water suppresses grain boundary cracking which has been shown to occur in the case of rapid cooling, i.e., quenching in cold water [19]. The samples were then aged at 225 °C for 4 h to form coherent nano-precipitates which are essential to improve plastic slip resistance and promote superelasticity. Following the CHT and aging heat treatments, the specimen surface was mechanically ground down to a grit size of 5 μm and vibropolished in 0.02 μm colloidal silica for 4 h. The microstructure was evaluated across the entire gauge section of each sample using electron backscatter diffraction

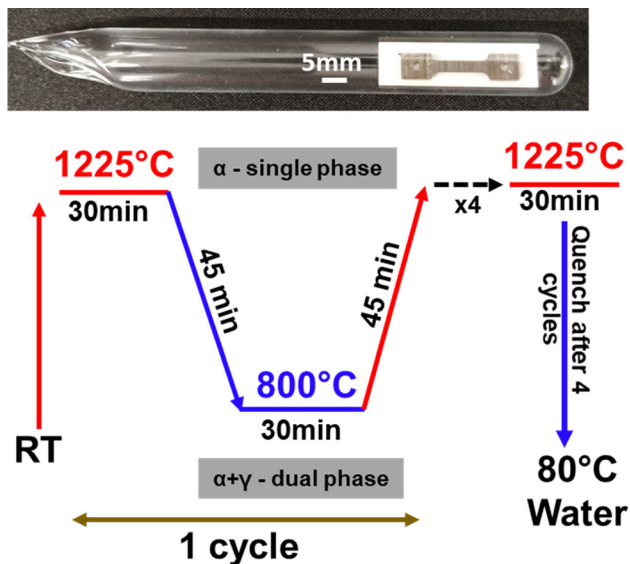


Fig. 1 Schematic of cyclic heat treatment resulting in AGG and a sample encapsulated in quartz tubing with argon is shown above the schematic

(EBSD). In all cases, the microstructure following CHT consisted of a single grain in the relevant specimen area. As can be seen by the superimposed EBSD images in Figs. 4 and 5, the loading direction was parallel to the $\langle 001 \rangle$ and the $\langle 013 \rangle$ crystallographic directions, respectively. Following microstructural characterization, samples dedicated to evaluating the tensile properties were prepared for full-field DIC measurements by applying a speckle pattern on the sample surface following the standard procedure detailed in previous studies [39]. The tensile tests were conducted using an Instron servo-hydraulic load frame equipped with an 11 kN load cell. The sample was loaded in displacement control at the rate of 0.02% per second and unloaded in stress control. A DIC reference image covering the entire sample gauge length was captured before deformation. During deformation, images were captured every 2 s.

After investigating the tensile properties, i.e., the superelastic strains in tension, of each sample, a notch with a width of 0.18 mm and 0.3 mm depth (perpendicular to the loading direction) was machined using wire EDM. The subsequent fatigue crack growth measurements were conducted at a load ratio of $R = 0.05$ and a frequency of 3 Hz. According to the transformation stresses revealed by the prior tensile tests, the peak stress for the $\langle 001 \rangle$ and the $\langle 013 \rangle$ oriented samples were set to 200 MPa and 275 MPa, respectively. Once a crack was visually identified, optical images for DIC analysis were captured for a single cycle at a rate of 15 frames per second with a resolution of 1600×1200 pixels ($1.25 \mu\text{m}/\text{pixel}$). By reducing the test frequency to 0.2 Hz for this measurement cycle, a

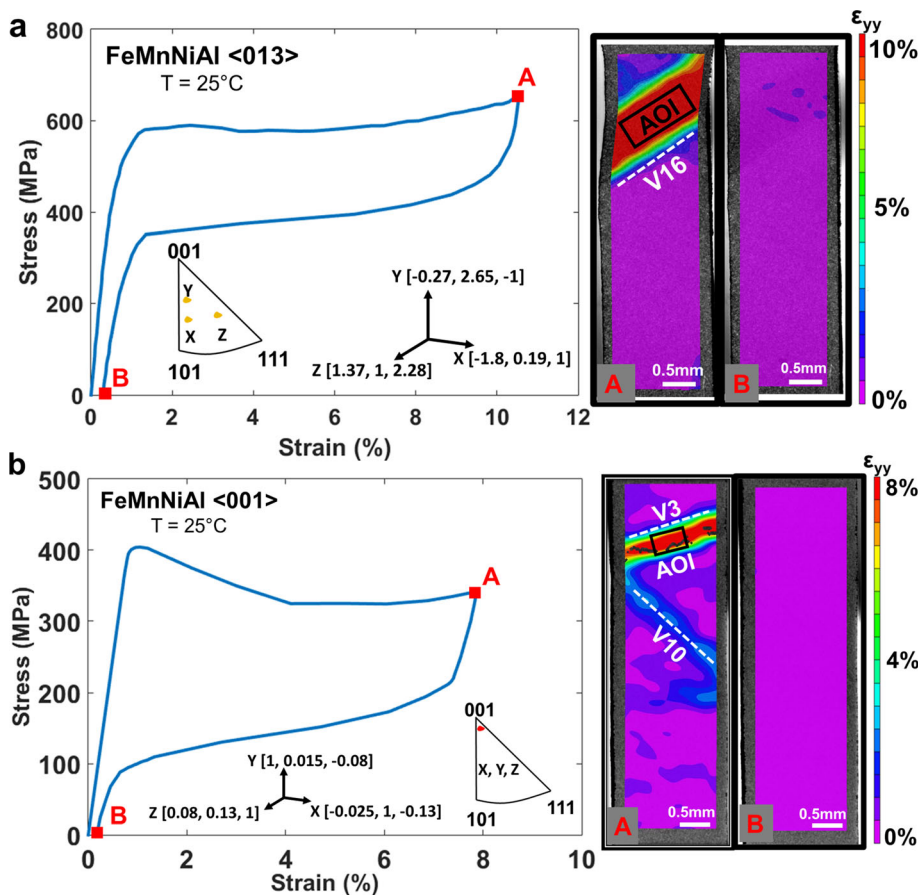
sufficient number of images for accurate regression analysis [40] could be obtained. Subsequent measurement cycles were conducted in intervals of 1,000 cycles. Full-field displacement measurements and strain calculations were obtained using commercial DIC software (VIC-2D, correlated solutions) applying a $64 \mu\text{m} \times 64 \mu\text{m}$ subset with a $6.3 \mu\text{m}$ step size. Linear least squares regression of the horizontal and vertical displacement contours near the crack tip allowed for the determination of the mode I and mode II stress intensity factors [40].

Results

Stress–Strain Response at RT

Figure 2 shows the stress–strain curves for the $\langle 013 \rangle$ and $\langle 001 \rangle$ oriented specimens. The result clearly points to excellent superelasticity and large magnitudes of recoverable strains (around 97% recovery for both orientations). The transformation stress for the $\langle 013 \rangle$ orientation was around 600 MPa with the maximum local transformation strain exceeding 10%. The DIC surface measurements point to the activation of a single martensite variant (single strain band as shown in Fig. 2a). The habit plane normal $\{0.1678 \ 0.7451 \ 0.6455\}$ and the transformation shear direction $\{-0.0356 \ 0.1579 \ -0.173\}$ for these martensite variants were established from the energy minimization theory [41, 42]. The stretch tensors for a BCC to FCC transformation used for the calculation were obtained using the lattice constants for austenite and martensite [13, 43]. See Appendix for the definitions of the variants V1, V2 etc. After establishing the habit plane variants, two-surface trace analysis of the TEM and SEM images was conducted to unambiguously determine this variant as variant 16 with the habit plane normal $[-0.6455 \ -0.7451 \ -0.1678]$ and a Schmid factor of 0.48 (for the details on these results the reader is referred to “[TEM Study of Martensite Variants](#)” of this chapter). In contrast, the $\langle 001 \rangle$ specimen exhibited a clearly lower transformation stress of 400 MPa with a maximum local transformation strain of about 8% only. Two variants, V3 and V10, with habit plane normal $[-0.7451 \ 0.1678 \ -0.6455]$ and $[-0.6455 \ -0.7451 \ 0.1678]$, respectively, and a Schmid factor of 0.49 were activated. We note that these results point to non-Schmid behavior [44] for transformation stresses because a quick calculation would reveal that the critical resolved shear stress (CRSS) for martensitic transformation is not the same for $\langle 013 \rangle$ and $\langle 001 \rangle$ as we discuss later in the study. The axial stress–strain data were used to calculate the anisotropic ratio of FeMnAlNi based on a simple, yet novel method. First, the Young’s moduli (E) of the austenite in the $\langle 013 \rangle$ and $\langle 001 \rangle$ orientations were determined from the stress–strain curves

Fig. 2 Stress–strain response of unnotched single crystals **a** $\langle 013 \rangle$ and **b** $\langle 001 \rangle$ orientations at RT is the plotted strains represent the local strain extracted from the AOI depicted in each image. Respective IPF maps, loading axis, and the DIC contours are shown



as 104.3 GPa and 61.5 GPa, respectively. The elastic compliance constant, S_{11} was subsequently obtained by using the elastic modulus and the direction cosines (l_i) of the $\langle 001 \rangle$ orientation in the equation for the orientation dependence of Young’s modulus in cubic crystals [45],

$$\frac{1}{E} = S_{11} - 2 \left(S_{11} - S_{12} - \frac{S_{44}}{2} \right) (l_1^2 l_2^2 + l_2^2 l_3^2 + l_1^2 l_3^2) \quad (1)$$

Subsequently, the anisotropic Poisson’s ratio ($-\epsilon_{xx}/\epsilon_{yy}$) for the $\langle 001 \rangle$ sample was experimentally determined from DIC at different load levels in the elastic loading regime. The resulting mean value of 0.42, as shown in Fig. 3, was used along with the expression for anisotropic Poisson’s ratio of $\langle 001 \rangle$ crystal orientation ($-S_{12}/S_{11}$) [46], for determination of S_{12} . Given S_{11} , and the ratio of S_{11} to S_{12} , S_{44} was obtained by substitution of the measured elastic modulus and direction cosines of $\langle 013 \rangle$ orientation in Eq. 1. The resulting stiffness and compliance values are reported in Table 1. The resulting anisotropic ratio, $2C_{44}/(C_{11} - C_{12})$, was 5.38 which is higher than NiTi (2.85) [47] and lower than CuZnAl (12) [48].

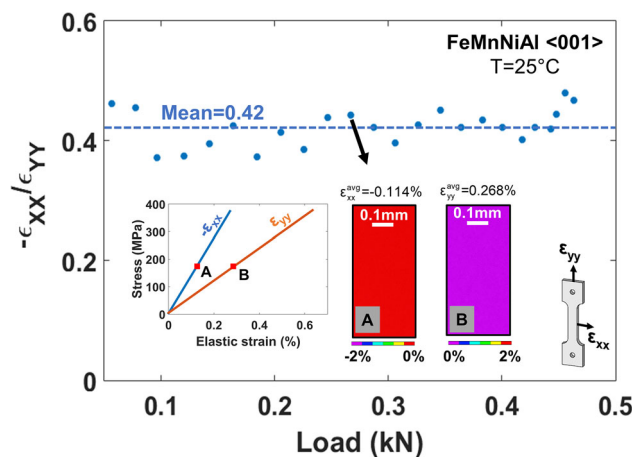


Fig. 3 Anisotropic poisson’s ratio for $\langle 001 \rangle$ FeMnNiAl plotted against load in the elastic regime. The average ϵ_{yy} and ϵ_{xx} strains shown in the DIC contours turn out to be 0.268 and -0.113 , respectively

Evolution of Residual and Recoverable Strain at the Notch Tip and Crack Wake

To identify the factors leading to crack initiation and crack advance, the strain fields were monitored at the notch tip and the crack wake, respectively. The strain history

Table 1 Elastic and Compliance constants for BCC Austenite FeMnNiAl

S_{11} (GPa^{-1})	S_{12} (GPa^{-1})	S_{44} (GPa^{-1})	C_{11} (GPa)	C_{12} (GPa)	C_{44} (GPa)	Anisotropic ratio
0.01667	− 0.00683	0.008881	139	97	113	5.38

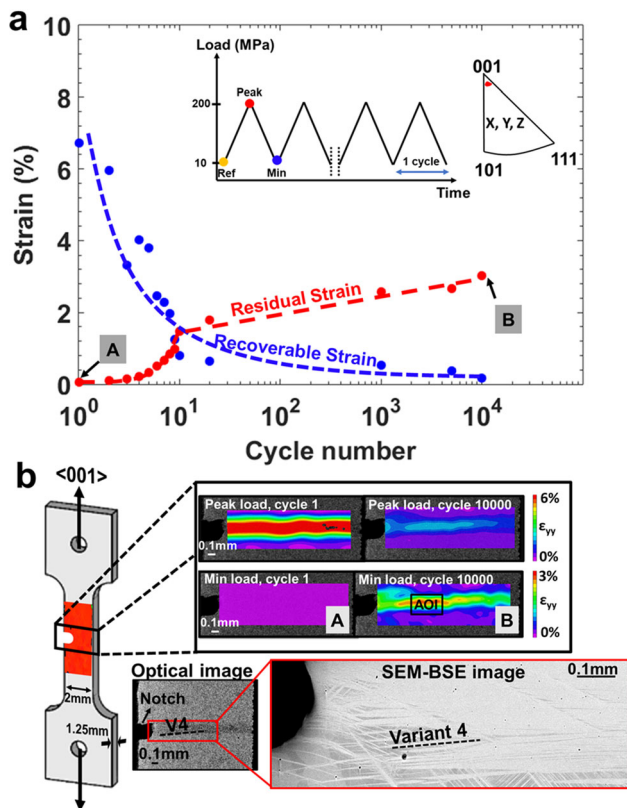


Fig. 4 **a** Strain history at the notch tip for $\langle 001 \rangle$ sample tracked for 10,000 cycles which shows the drastic reduction in superelastic strains and formation of residual strains. **b** Standard dog bone sample used for this test overlaid with EBSD map and the DIC strain contour ahead of the notch for cycles 1 and 10,000. Below the DIC contours are the optical image of the DIC surface and the corresponding SEM-BSE image indicating high volume fraction of residual martensite at the notch tip. Note that sub-critical crack growth was not achieved in this orientation due to catastrophic failure

obtained from DIC at the notch tip of the $\langle 001 \rangle$ oriented sample revealed local recoverable strains of 7% in the first cycle (Fig. 4). However, within the first 10 cycles, these strains drastically declined to below 1%, while the residual strain exceeded 1.5%. With continued cycling of the sample to 10,000 cycles, the superelastic strain further decreased to less than 0.5%, while the residual strain reached 3%. The full-field strain contour plots shown in Fig. 4b show clear localization of strains to a narrow horizontal band in the direct vicinity to the notch. The habit plane normal, determined via trace analysis, for the activated variant belongs to variant 4 (V4) $[-0.7451 \ 0.1678 \ 0.6455]$ and the corresponding Schmid factor is 0.48. As shown in Fig. 4b, the strain level at peak load is clearly

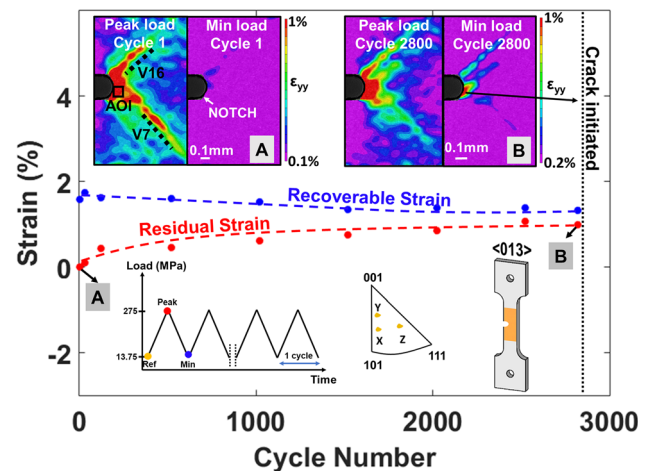


Fig. 5 Strain history at the notch tip for $\langle 013 \rangle$. Strains were averaged from the AOI shown in the DIC contours. Insets feature the DIC strain contours, IPF map, loading schematic and notched dog bone sample overlaid with EBSD map. Location of crack initiation location is pointed out in the top right DIC image

higher in the beginning of the test than after 10,000 cycles. In the same interval, the strains at minimum load significantly increase, which is in good agreement with the development of irrecoverable and residual strains as described above. The optical and SEM images in Fig. 4b show that the area of increased strains is composed of several interacting martensite variants, with a major contribution from variant 4. The fatigue crack growth could not be studied in $\langle 001 \rangle$ sample because upon fatigue crack initiation, the sample failed catastrophically.

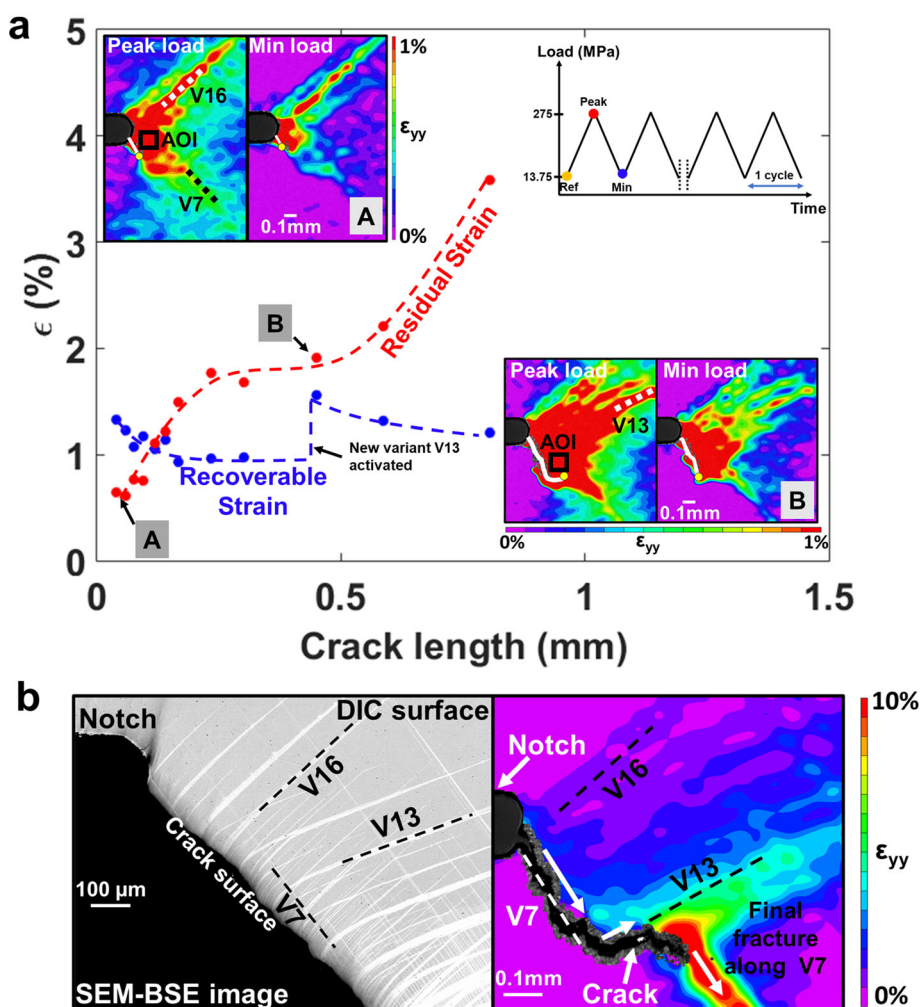
The results from local strains analysis of the notch tip of the $\langle 013 \rangle$ oriented sample are presented in Fig. 5. Deterioration of the recoverable strain is evident, as is the accumulation of residual strain. However, although the general trends are the same as in case of the $\langle 001 \rangle$ orientation, the deterioration is more gradual (note that strains are plotted for 3000 cycles only). Likewise, the strain distribution appears different to that observed for the $\langle 001 \rangle$ orientation. Thus, the volume of highly strained zone spans over a larger domain and shows the activation of two variants, V16 and V7, with the habit plane normal $[-0.6455 \ -0.7451 \ -0.1678]$, $[-0.7451 \ 0.6455 \ -0.1678]$ and a Schmid factor of 0.43 and 0.49, respectively. Variants were identified via trace analysis. Again, the strains at peak and minimum load in the beginning of the test and after 2,800 cycles can be clearly correlated to the development of recoverable and residual strains shown

in the graph. A crack was identified in the AOI at the notch tip of the $\langle 013 \rangle$ sample as the residual strain exceeded 1% at the mark of 2800 cycles. The location is indicated in the top right DIC image in Fig. 5.

As the crack advanced, the recoverable strains and the residual strains in the crack wake were extracted from DIC for various crack lengths (Fig. 6). The recoverable superelastic strains start out at 1.3% in the short crack regime (0.04 mm) and gradually decrease to 1% as the crack advances. When the crack length is around 0.48 mm, a sudden increase in the superelastic recoverable strain is observed. This increase coincides with formation of a new variant (cf. DIC image corresponding to point B in Fig. 6a and the BSE image recorded post-mortem in Fig. 6b). Trace analysis indicated this variant to be V13 with habit plane normal $[-0.1678 - 0.7451 0.6455]$. In course of further cycling, the recoverable strain decreases again accompanied by an increase of residual strain. As the crack continues to grow, new areas of the material transforms, which leads to residual strain in the crack wake exceeding 2.5%. The DIC contours shown in Fig. 6a and b depict the

crack path (indicated by the solid white line in Fig. 6a) and the strain field around the crack. As the area of increased strains is limited to one side of the crack, a clearly asymmetric transformation with respect to the crack plane is observed. As the crack propagates, i.e., throughout the entire test, the material both ahead of the crack tip and in the crack flank transforms. Variants V16 and V13 are active in the crack flanks, whereas variant V7 is active ahead of the crack tip. The crack propagated approximately parallel to variant 7—the trace of the crack plane angled at approximately 63° with respect to the horizontal, and the trace of the variant V7, was inclined at 58° , match to a close degree. Although the crack is deflected towards V13 at a crack length of about 0.7 mm, V7 remains dominant for influencing the crack growth direction. Eventually, the strain at the crack tip exceeds 10% and final fracture is observed mostly parallel to V7 (cf. DIC contour in Fig. 6b).

Fig. 6 a Residual strain and recoverable strain in the crack wake vs. crack length for FeMnNiAl $\langle 013 \rangle$. Note the increase in residual strain and recoverable strain after the activation of a new variant when the crack reaches a length of 0.48 mm. Loading schematic and DIC strain contours are shown as insets b Post failure SEM image on the left showcasing multiple variants responsible for crack growth and DIC contour on the right capturing the crack path and the activated variants on the crack flanks when the crack is 1.15 mm long. It clearly indicates the pivotal role of variant 7 in crack propagation and final fracture



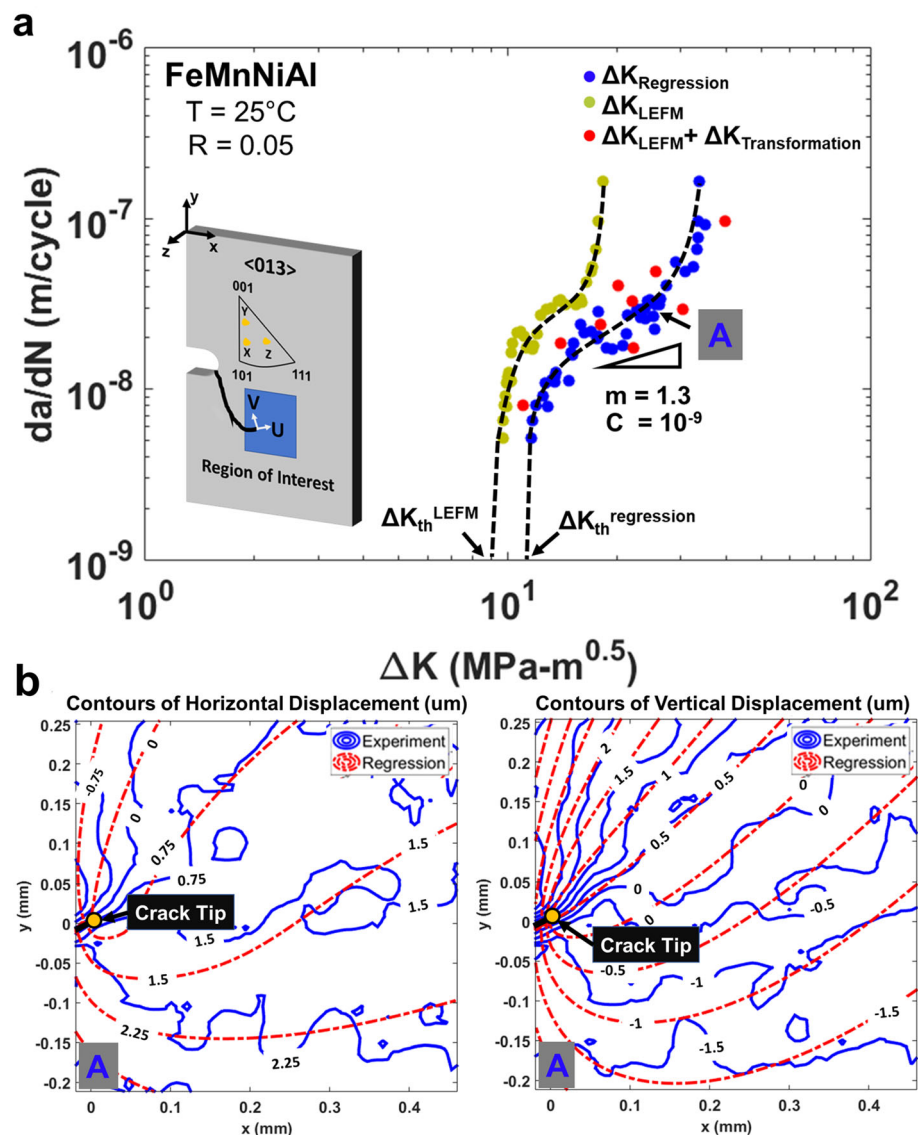
Fatigue Crack Growth Behavior

The classical LEFM solution for the stress intensity factor is obtained from handbook solutions [49]. The LEFM fatigue crack growth curve is represented by yellow dots as shown in Fig. 7a. The critical stress intensity factor at fracture and the threshold stress intensity represent the bounds on the fatigue crack growth data. A threshold stress intensity of about $9 \text{ MPa m}^{0.5}$ was obtained for $\langle 013 \rangle$ oriented FeMnAlNi. However, it must be noted that the crack path deviates substantially from the horizontal crack path leading to a substantial contribution from Mode II stress intensity. So, it is imperative to obtain both ΔK_I and ΔK_{II} from the measured displacements. In the first step, we execute a least squares regression fitting of the measured horizontal and vertical displacement contours to an analytical anisotropic solution [50]. The detailed procedure for

the regression method has been illustrated previously for non-transforming [40, 51] and transforming materials [33, 35] and, thus, is not further described here. Figure 7b shows the experimental displacement contours in horizontal and vertical direction together with the theoretical regression fit. A good agreement between the experimental and theoretical fit is evident and consistent throughout the entire analysis. The total stress intensity factor for mixed mode crack growth is then (in the second step) calculated by incorporating the ratio of mode I and mode II energy release rates (cf. Eqs. 8, 9 and 10). The resulting ΔK is plotted against the measured crack growth rate in Fig. 7a (blue dots). Regression analysis reveals a drop in the crack growth rate (da/dN) when the stress intensity at the crack tip is in the range of 17 to 22 $\text{MPa m}^{0.5}$.

According to the data obtained by DIC, the $\langle 013 \rangle$ orientation exhibits threshold stress intensity range of

Fig. 7 **a** LEFM and regression stress intensity factors plotted against the crack growth rate. **b** Experimental horizontal and vertical displacement contours plotted along with the regression fit for a crack length of 0.65 mm with a stress intensity of $30 \text{ MPa m}^{0.5}$ (point A in **a**)



11 MPa m^{0.5}, while the critical stress intensity range is 40 MPa m^{0.5}. The slope of the Paris regime (stage II) is approximately 1.3. It is evident that the crack tip stress intensities obtained by the regression analysis is clearly higher than the LEFM solution. A micromechanical analysis was conducted to evaluate the effective stress intensities as a modification of the LEFM solution. This analysis indeed shows a phenomenon which was termed deshielding [36], i.e., the local driving forces exceed that determined on the basis of LEFM. This may be due to the highly asymmetric nature of the transformation zones producing a substantial Mode II stress intensity component. Despite this deshielding effect, the complexity associated with the activation of new variants with corresponding superelasticity imparts material resistance. So, the resulting fatigue crack growth rates exhibit a rather low Paris exponent which points to favorable fatigue crack growth properties. To understand the role of competing effects, we undertake a calculation of the stress intensity change considering the local driving forces in the following section.

Calculation of ΔK Change Attributed to Asymmetric Transformation

The ΔK due to the transformation was calculated by employing a McMeeking–Evans–Eshelby-type methodology which was formerly used to derive the crack wake tractions in transforming ceramics [52, 53]. However, in our case, we note the presence of asymmetric transformation zones which needs to be considered in our calculations of effective stress intensity (Fig. 8).

The constrained stress (tractions) which arise due to internal transformation strain can be calculated using the

equivalent inclusion method [54]. The strain measured via DIC ($\epsilon^{\text{tot-DIC}}$) includes both the constrained (transformation) strain and the far field elastic strain (ϵ^{far}). So, the intrinsic eigenstrain (ϵ^{int}), i.e., the theoretical strain for transformation, without the constraint from the surrounding matrix, is calculated as [55],

$$\epsilon_{ij}^{\text{int}} = S_{ijkl}^1 (\epsilon_{kl}^{\text{tot-DIC}} - \epsilon_{kl}^{\text{far}}) \tag{2}$$

where S_{ijkl} is the Eshelby’s tensor [55]. At maximum load where the transformation at the crack tip occurs, modulus mismatch between the austenite and martensite needs to be considered. Thus, the equivalent eigenstrain (ϵ^{**}), which is the sum of the strain due to the modulus mismatch between austenite and martensite and the intrinsic eigenstrain, is calculated using Eshelby’s equivalent inclusion method for inhomogeneous media [55],

$$C_{ijkl} \left(\epsilon_{kl}^{\text{far}} + S_{klmn} \epsilon_{mn}^{**} - \epsilon_{kl}^{**} \right) = C_{ijkl}^* \left(\epsilon_{kl}^{\text{far}} + S_{klmn} \epsilon_{mn}^{**} - \epsilon_{kl}^{\text{int}} \right) \tag{3}$$

where C_{ijkl} and C_{ijkl}^* are the elastic constants of austenite and martensite, respectively. After determining the equivalent eigenstrain, the elastic internal stresses developed at the transformation zone boundary is given as, [35, 38, 52, 55]

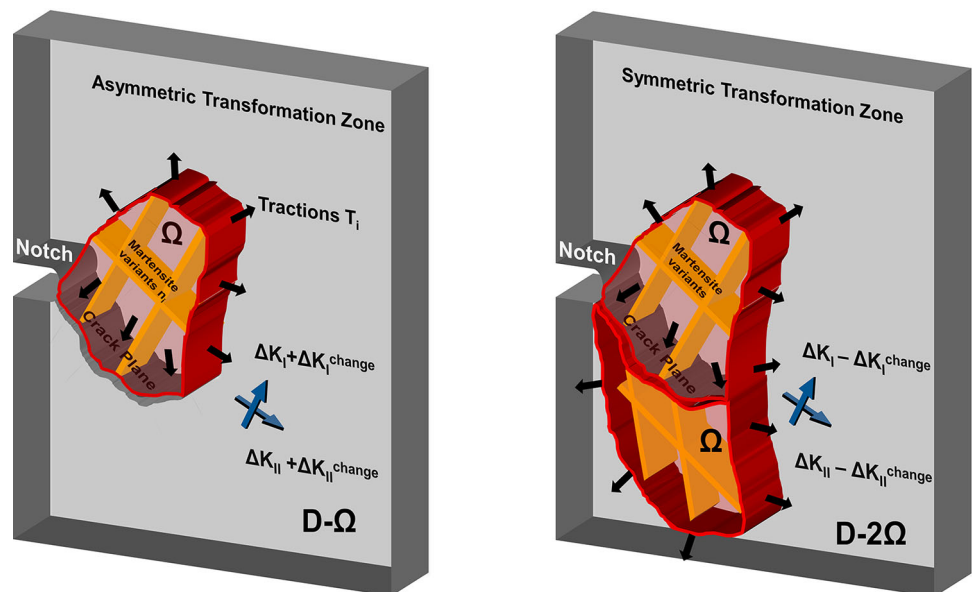
$$\sigma_{ij} = C_{ijkl} (S_{klmn} \epsilon_{mn}^{**} - \epsilon_{kl}^{**}) \tag{4}$$

Now, the surface tractions in the transformation zone boundary is given by,

$$T_i = \sigma_{ij} n_j \tag{5}$$

where n_i is the normal of the martensite variant obtained through two-surface trace analysis in the crack coordinate

Fig. 8 Schematic of the asymmetric transformation observed in FeMnNiAl. Depending on the crystal orientation the transformation zone pattern can differ. The <013> case studied in this work corresponds to the asymmetric zone. The shear and normal tractions are depicted in this schematic. Depending on whether the transformation zone is symmetric or asymmetric, the shear tractions on the crack flanks can result in a decrease or increase in the mode II stress intensity factor, respectively



frame depicted as $x'y'z$ in Fig. 11, where the shape of the transformation zone is taken as a rectangle. With the calculated surface tractions, the mode I and mode II components of $\Delta K_{\text{transformation}}$ can be calculated following the weight function methodology by Bueckner [56] and Rice [57].

$$\Delta K_I^{\text{transformation}} = \int (T_{x'} h_{Ix'} + T_{y'} h_{Iy'}) dS_p \tag{6}$$

$$\Delta K_{II}^{\text{transformation}} = \int (T_{x'} h_{IIx'} + T_{y'} h_{IIy'}) dS_p \tag{7}$$

where $h_{x'}$ and $h_{y'}$ are the anisotropic weight functions and dS_p is the line element of the zone perimeter. Note that asymmetric tractions ($T_{x'}$ and $T_{y'}$) give rise to substantial increase in ΔK_{II} . Rice [57] showed that the weight functions can be derived from analytical expressions given by Sih [50] for displacement fields (u, v) and the stress intensity factors K in reference loading coordinate system (see Appendix).

The calculated mode I and mode II components of $\Delta K_{\text{transformation}}$ were added to the mode I and mode II components of ΔK_{LEFM} . Thus, the total ΔK for mixed mode crack growth is calculated as [36, 51],

$$\begin{aligned} &\Delta K^{\text{LEFM}} + \Delta K^{\text{transformation}} \\ &= \sqrt{(\Delta K_I^{\text{LEFM}} + \Delta K_I^{\text{transformation}})^2 + \alpha(\Delta K_{II}^{\text{LEFM}} + \Delta K_{II}^{\text{transformation}})^2} \end{aligned} \tag{8}$$

where α is the ratio between the energy release rates in mode II and mode I, J_2/J_1 , which are given as [50],

$$J_1 = -\frac{\pi K_I}{2} a_{22} \text{Im} \left[\frac{K_I(\mu_1 + \mu_2) + K_{II}}{\mu_1 \mu_2} \right] \tag{9}$$

$$J_2 = -\frac{\pi K_{II}}{2} a_{11} \text{Im} [K_{II}(\mu_1 + \mu_2) + K_I \mu_1 \mu_2] \tag{10}$$

Using the definitions of μ_1 , μ_2 , a_{11} and a_{22} , as given in the Appendix, values in the range of 2.1 to 2.9 were obtained for α . The final K contribution obtained from integrating the traction forces produces a $\Delta K_{\text{transformation}}$ which is shown together with the obtained total stress intensity in Table 2 for a crack length of 0.48 mm. Contemplating the total obtained for mode I and mode II, a

clearly higher contribution from the latter becomes apparent. It is evident from Fig. 7a, that the calculated effective $\Delta K (= \Delta K_{\text{LEFM}} + \Delta K_{\text{transformation}})$ is nearly the same as $\Delta K^{\text{regression}}$.

TEM Study of Martensite Variants

After FCG experiments, TEM specimens were extracted from the $\langle 013 \rangle$ sample and the results are presented in Fig. 9. Focused ion beam milling technique was employed to prepare the lamellae for TEM. Thermo Scios 2 dual beam SEM–FIB and JOEL 2100 Cryo TEM were used for the sample preparation and analysis, respectively. The recorded selective area diffraction patterns from the regions marked as DP1 and DP2 in Fig. 9a and c indicate an FCC martensite and BCC austenite. The typical internally twinned structure is noticeable in Fig. 9b. Due to the limitation of the maximum achievable tilting angle in the TEM, the diffraction conditions were not met to clearly resolve the dislocation lines in Fig. 9c and b. However, upon close inspection at the A/M interface in Fig. 9b, some dislocation loops (indicated by black arrows) are visible, whereas in Fig. 9c, dark contrast at the A/M interface is from dislocations but the individual dislocation lines could not be resolved due to the reason mentioned before. Additionally, two-surface analysis was conducted on traces of variants observed in BSE-SEM image in Fig. 9d and the corresponding FIB lamellae #1 and #3 to unequivocally established the orientation of the variants which got activated and influenced the crack propagation in the $\langle 013 \rangle$ orientation.

Discussion

Based on the reported experimental results and subsequent analysis, it is instructive to discuss the variant activation and strain localization affecting the crack nucleation (“Orientation Dependency of Strain Localization: $\langle 001 \rangle$ vs $\langle 013 \rangle$ —Its Role in Crack Initiation” section) and subsequently fatigue crack growth (“Activation of Variants in

Table 2 Stress intensity factors arising from the surface tractions imposed on the different zone boundaries due to transformation

Zone	$\Delta K_I^{\text{transformation}}$ (MPa m ^{1/2})	$\Delta K_{II}^{\text{transformation}}$ (MPa m ^{1/2})
1	– 1.52	0.42
2	– 2.80	1.66
3	2.24	1.73
4	2.54	3.21
Total	0.46	7.02
$\Delta K_{\text{LEFM}} + \Delta K_{\text{transformation}}$	4.26	12.85
$\Delta K_{\text{regression}}$	5.94	11.78

Crack length is around 0.3 mm and w/a is 0.5

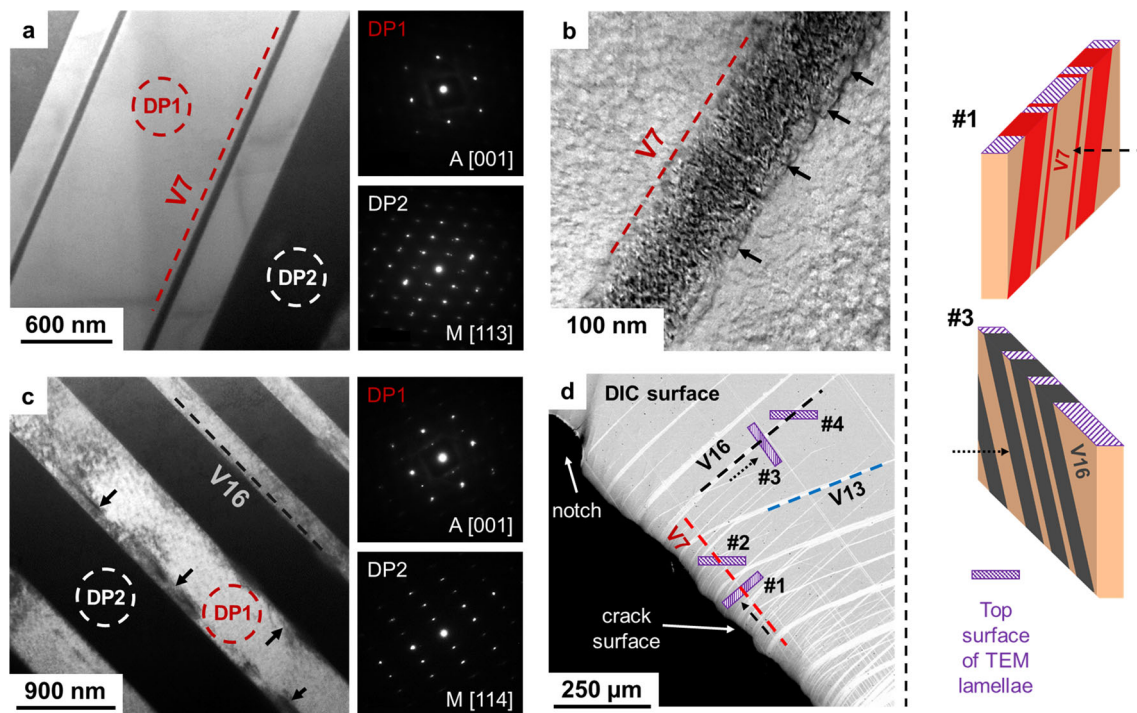


Fig. 9 **a** Bright-field image of lamella #1 showing V7 within the austenitic matrix. The diffraction pattern stemming from the areas marked by the dashed circles DP1 and DP2 are given to the right. **b** At higher magnification and different tilting angle, the internally twinned structure of martensite in FeMnAlNi is perceptible within lamella #2. The dislocation loops at the A/M interface are pointed out with the black arrows. **c** V16 is shown in the bright-field image stemming from lamella #3. Irrespective of the relatively large distance to the crack, dislocation activity seems to be pronounced, which can be deduced from the dark areas in the austenitic region in

direct vicinity to the austenite–martensite interface (black arrows). SAED pattern stemming from the areas indicated by the dashed circles are also given to the right. Subimage **d** shows a BSE image of the failed specimen and the orientation of TEM samples relatively to the crack. Distances and TEM lamella dimensions are qualitatively only. The schematics to the right highlight the orientation of V7 and V16 within lamellae #1 and #3, respectively. The direction of view in images **a** and **c** is marked by the dashed and dotted arrows, respectively

“**⟨013⟩ Case During Fatigue Crack Growth**” section). We then introduce the concepts of asymmetric transformation zone resulting in deshielding effects in FeMnNiAl (“**Fatigue Crack Growth in ⟨013⟩ Orientation: Effect of Asymmetric Transformation**” section).

Orientation Dependency of Strain Localization: ⟨001⟩ vs ⟨013⟩—Its Role in Crack Initiation

The results presented in Figs. 4 and 5 highlight the considerable difference between the ⟨013⟩ and ⟨001⟩ orientations in terms of strain levels and activated variants ahead of the notch. The initial recoverable strain ahead of the notch in ⟨013⟩ was only 2% compared to 8% for the ⟨001⟩ case. However, even though the ⟨001⟩ orientation exhibited higher local superelastic strain initially, its functional performance was relatively inferior as the recoverable strain magnitudes deteriorated rapidly under cyclic loading and saturate at only 1% recoverable strain. The high strain in ⟨001⟩ case is consistent with theoretical transformation strain calculations [22] which point to magnitudes near

10%. However, such high transformation strains are not sustained upon cycling as the same variants are activated cycle after cycle resulting in the accumulation of dislocation slip and eventually loss of functionality. The source of dislocation mediated plasticity emanating from the variant(s) is twofold: (i) the internal twinning of the martensite is accomplished by twinning dislocations, and (ii) the misfit at the A/M interface (habit plane) is accommodated by dislocations. The forward/reverse movement of the A/M interface during transformation leads to dislocation emission into the austenite matrix [27, 58] which can be inferred from Fig. 9. In addition to the above observations, the slip resistance in FeMnNiAl must depend on orientation as well (i.e., non-unique CRSS) but a quantitative description is not available at this time. In alloys such as NiTi, the slip resistance is significantly above the transformation stress but in FeMnNiAl the slip resistance is very similar to the transformation stress [19, 22]. Further work is needed to understand the slip stress magnitude with respect to transformation stress, but this is outside the scope of this study.

Furthermore, we note that the results presented in Fig. 2 imply a strong non-Schmid response of transformation stress, i.e., the CRSS for transformation is 190 MPa for $\langle 001 \rangle$ and 280 MPa for $\langle 013 \rangle$ (in both the cases the Schmid Factor for the activated variant was 0.48). Non-Schmid response has been observed in Fe_3Al [59, 60], NiTi [61] and CuZnAl [62] but not well studied for other SMAs. However, under a given external stress magnitude, this orientation dependence and dissimilar transformation stress levels can clearly induce transformation strain magnitudes at the notch that are far higher in the $\langle 001 \rangle$ case compared to $\langle 013 \rangle$ orientation. This is consistent with the large strains/martensite volume fraction observed for the $\langle 001 \rangle$ case (Fig. 4) compared to the isolated martensite bands (low volume fraction) in the $\langle 013 \rangle$ case (Fig. 6). Also, in the case of the notched and cracked specimens, the prevailing stress state differs from the uniaxial case, thus activating different variants (compare Fig. 2 to Figs. 4 and 6) and contributing to different transformation strains as revealed by digital image correlation.

From Fig. 4a, it is evident that even with the accumulation of residual strains of above 2.5%, the $\langle 001 \rangle$ orientation exhibited excellent resistance to crack initiation for over 10,000 cycles. Apparently, in this case the crack nucleation occurs in a primarily residual martensite domain (Fig. 4b) which is known to exhibit superior fatigue resistance [32, 63, 64] compared to austenite. On the contrary, in the $\langle 013 \rangle$ orientation the crack nucleation occurred after 2800 cycles when the residual strain just exceeded 1% in a primarily austenite matrix where austenite–martensite interfaces are present (Fig. 6(b)). Superior resistance to fatigue crack initiation in $\langle 001 \rangle$ orientation comes at an expense because this orientation suffers cleavage fracture upon crack nucleation ($\langle 001 \rangle$ is a cleavage plane for BCC materials [65, 66]). Consequently, and unlike the $\langle 013 \rangle$ orientation, the $\langle 001 \rangle$ crystal is not suitable for fatigue crack growth investigation.

Activation of Variants in $\langle 013 \rangle$ Case During Fatigue Crack Growth

Considering the strain contours of the $\langle 013 \rangle$ sample in Fig. 5, it is evident that at least two dominant variants were active at the notch tip (compared to single dominant variant in the $\langle 001 \rangle$ case). It should be noted that once the dominant variant undergoes functional fatigue, it no longer exhibits the local superelasticity observed in the first cycle. Subsequent cycles exhibit lower levels of superelastic strains and gradually transitions into a plastic response as clearly shown in Fig. 10. Once a fatigue crack eventually initiated at the notch tip, the damage location was found to coincide with the A/M interface of variant 7 as shown in Fig. 5. As the crack advances, the stress state at the crack

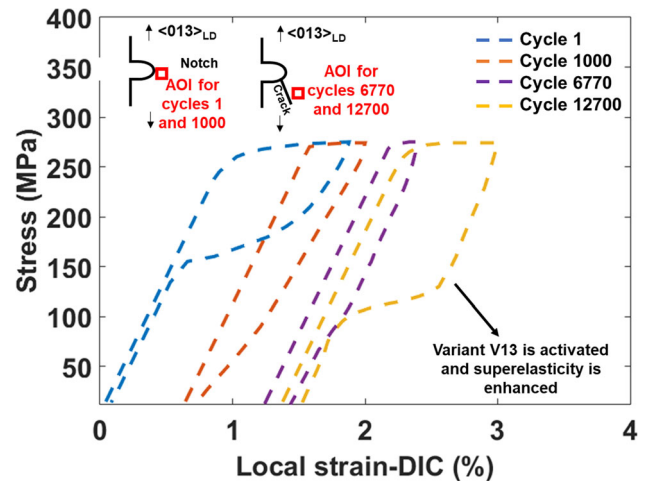


Fig. 10 Global stress vs local strain curve. The local strains prior to crack initiation, i.e., cycles 1 and 1000 were extracted from the notch tip and the local strains after crack initiation, i.e., cycles 6770 and 12,700 were extracted from the crack flank. Stress–strain curve for cycle 6770 depicts elasto-plastic behavior with $\sim 1\%$ strain recovery and superelastic behavior is enhanced with $\sim 1.5\%$ strain recovery in cycle 12,700 as a new variant is activated near the crack tip. This also results in crack deflection and a reduction in the crack growth rate (Fig. 6 depicts crack deflection and Fig. 7 depicts the transient reduction in crack growth rate)

tip results in the activation of a new variant and restores the superelastic behavior at the crack tip (Fig. 10). Then, the martensite spreads to previously untransformed domains ahead of the crack as illustrated with external stress–local strain curves in Fig. 10 and in Fig. 6a which points to restored local superelasticity once variant V13 is activated. As noted earlier, this superelastic response produces transient retardation of fatigue crack growth rates and impacts the trajectory of crack growth. From the DIC contour plots and SEM/TEM images, it is evident that the crack trajectory (sometimes in a zig-zag way) is dictated by the successive activation of different variants around the crack tip and plastic deformation near the associated interfaces.

Fatigue Crack Growth in $\langle 013 \rangle$ Orientation: Effect of Asymmetric Transformation

Fatigue crack growth experiment conducted on a $\langle 013 \rangle$ oriented sample has shown that this orientation exhibits an unusually high threshold stress intensity factor of $11 \text{ MPa m}^{0.5}$, one of the highest among the SMAs currently being studied. As stated above, exhaustion of a variant and the activation of a new variant(s) are developed during fatigue crack advance impacting threshold fatigue crack growth resistance. In comparison, NiTi [32, 33] and CuZnAl [36] exhibit threshold around $1\text{--}3 \text{ MPa m}^{1/2}$ while Ni₂FeGa [35] has a threshold value around $8 \text{ MPa m}^{1/2}$. The critical stress intensity range for fatigue failure in

$\langle 013 \rangle$ FeMnNiAl is near $40 \text{ MPa m}^{1/2}$ in comparison to $17 \text{ MPa m}^{1/2}$ for CuZnAl [35], $35 \text{ MPa m}^{1/2}$ for NiTi [32] and $23 \text{ MPa m}^{1/2}$ for Ni₂FeGa [35]. Previous studies have reported a threshold levels of $5\text{--}9 \text{ MPa m}^{0.5}$ for 304 steels [67], $9 \text{ MPa m}^{0.5}$ for 2.25Cr-1Mo steel [68], $5\text{--}12 \text{ MPa m}^{0.5}$ for 0.55C-2.23Mn pearlitic-martensitic steel [69], $8.5 \text{ MPa m}^{0.5}$ for 300-M high strength steel [68], $11 \text{ MPa m}^{0.5}$ for austenitic Fe-29Ni-17Al transforming alloy [63] and $11\text{--}12 \text{ MPa m}^{0.5}$ for ferrite-pearlite steels [70]. It is thus evident that the intrinsic threshold stress intensity factor for FeMnNiAl is comparable to many high strength structural steels, which can be attributed to the nature of superelastic transformation taking place near the crack tip as discussed below.

The stress intensity at the crack tip arises from the applied external load and internal tractions developing due to reasons such as phase transformations. The offset between the LEFM solution, and the regression results portrayed in Fig. 7 may stem from the asymmetric transformation experienced by FeMnNiAl in this orientation as discussed further. $\Delta K^{\text{regression}}$ shown in Fig. 7a, takes into consideration the stress intensities arising from applied external load and internal tractions. If the internal tractions contribute a negative ΔK change, the allowable external load is increased like in the case of stabilized ceramics where significant volume expansion during phase transformation [52, 53] imparts compressive traction on the crack flanks. On the other hand, if the internal tractions resulted in a positive contribution to the stress intensity change, the allowable external load is decreased. In case of FeMnNiAl in this study, the asymmetry of the phase transformation with respect to the upper and lower part of the crack could physically manifest as uneven shear tractions on the crack flanks resulting in a positive Mode II contribution to the crack tip stress intensity change as reported in Table 2. This is in contrary to the negative ΔK contribution from the symmetric phase transformation observed in Ni₂FeGa [35] SMA, where only Mode I contribution was significant. This negative contribution acts as an intrinsic crack shielding mechanism for ceramics and SMAs. However the asymmetric transformation which is also observed in CuZnAl [36], acts as an intrinsic crack deshielding mechanism due to the increase in the net crack tip driving force. Fewer lattice correspondences and high elastic anisotropic ratio in this SMA affects the localization of crack tip phase transformation. FeMnNiAl SMA has 3 lattice correspondences and the anisotropy ratio is 5.38 compared to NiTi which has an anisotropic ratio of 2.85 [47] and 12 lattice correspondences. CuZnAl also has 12 lattice correspondences, but the anisotropic ratio is 12 [48] and the degree of deshielding is higher [36]. In a broader sense, asymmetry in transformation is a consequence of the orientation of the sample which dictates what variants

are activated and thus the crack initiation and the crack propagation path. It's also worth noting that the transients in the crack growth rate observed over a range of stress intensities in the da/dN vs ΔK curve depicted in Fig. 7a, coincides with the activation of variant 7 and 13 ahead of the crack tip resulting in the increase in crack surface roughness upon crack path deflection lowering the fatigue crack growth rates near the threshold. This type of a crack retardation was observed in austenitic steels exhibiting stress induced martensitic transformation at the crack tip [63] and resulted in a $da/dN\text{--}\Delta K$ curve with a similar oscillatory shape.

Factors Governing the Fatigue Crack Growth Response in Shape Memory Alloys

The exhaustion of functionality of a superelastic SMA always occurs in conjunction with plastic deformation [71, 72] at the A/M interface. Such degradation in superelasticity dictates the structural fatigue properties of the SMA. Irreversibility in transformation stemming from dislocation pinned A/M interfaces creates strain localization in the material which leads to crack initiation. Crack advance has been typically observed to occur parallel to a preferred variant, i.e., along the austenite/martensite interfaces. Stress state at the crack tip activates phase transformation which influences the crack trajectory. Depending on the anisotropy ratio of the material, loading orientation and lattice correspondences, the transformation in the crack tip process zone is either symmetric or asymmetric. Typical stress induced irreversible martensitic transformation in a ferrous alloy is accompanied by a volume change which induces compressive normal tractions on the crack flanks. Whereas in ferrous SMAs which undergoes reversible phase transformation, the volume change is small and thus the compressive tractions are small. However, the accompanied large shear displacements in asymmetric phase transformations with respect to the crack plane induce additional uneven shear tractions on the crack flanks which can increase the net local driving forces.

As a concluding remark, to enhance the structural and functional fatigue properties of Fe-based SMAs, the reverse movement of A/M interface without the formation of defects/dislocations is critical. Through experimental observations of monotonically loaded Fe-based SMAs, Kajiwara [27] concluded that dislocations at A/M interface can be reduced by achieving relatively small twin width in the martensite by lowering the twin boundary energy. Bhattacharya [73] et al., through numerical simulations, reached a conclusion that BCC to FCC transformation has no group-subgroup relationship and hence leads to the formation of defects like dislocations which affects the

reversibility. Later in 2017, Gao et al. [74] argued that even if the austenite and martensite have a group-subgroup relationship, MT results in defect formation due to symmetry breaking while cycling between the parent and product crystal structures. Thus, to address these issues the crystal structure of the martensite for Fe-based SMAs with a relatively low twin boundary energy in the internally twinned martensite would be desirable as pointed out by Kajiwara through experimental observations [27] and by Mohammed et al. via MD simulations [75]. This can be achieved by suitably tailoring the lattice constants in the present FeMnNiAl alloy system by altering the compositions of the alloying elements to induce a cubic to tetragonal austenite to martensite phase transformation, rather than a BCC to FCC transformation and thereby reducing the magnitude of dislocation slip vectors at the A/M interface. In conjunction to this, these studies also concluded that, at the temperature of deformation, the critical stress for slip should also be much higher compared to the stress required to induce phase transformation. Given that FeMnNiAl exhibits relatively low Clausius Clayperon slope [17, 18], it could be worth to study the superelasticity of this alloy under fatigue at cryogenic conditions where the slip stress would be considerably higher. This can open up new applications for these class of alloys.

Conclusions

The following conclusions can be drawn from this study:

- The results show that the transformation stress is strongly orientation dependent deviating significantly from the Schmid Law with [013] showing higher CRSS compared to [001]. The activated variants differ upon comparison of the unnotched and notched cases pointing to the role of stress state effects on transformation. Upon exhaustion of recoverable strains in a particular variant another favorably oriented variant is activated resulting in crack retardation.
- Depending on the nature of transformation ahead of crack tips, the crack tip driving forces are modified and affected by the asymmetry of the transformation fields. Such a calculation permits comparison of local driving forces with that based on stress intensity handbooks. Such a comparison allows intrinsic threshold levels to be established.
- Intrinsic threshold stress intensity for FeMnNiAl in this study is on the order of $11 \text{ MPa m}^{0.5}$ which exceeds the levels in non-transforming alloys. Despite this high threshold level, the range of stress intensity prior to fracture was limited to $40 \text{ MPa m}^{0.5}$.
- TEM results via two-surface analysis unequivocally confirmed the prevailing martensite variants. The orientation of the variants coincided with the phenomenological theory. During fatigue crack growth, several martensite variants are activated at the crack front which become stabilized as crack advances and remain in the crack wake.
- The DIC results showed considerable localization and activation of new variants. It was observed that these variant boundaries can act as sites for crack initiation. Subsequent crack propagation occurs along these variants. The stress state at the crack tip activates new variants as the crack progresses which influence the crack trajectory and crack propagation rate.

Acknowledgements We would like to thank Dr. Xiangyang Zhang for helping with the habit plane calculations. This work is funded by the National Science Foundation DMR Grant 1709515 Metallic Materials and Nanomaterials Program. EBSD and TEM/FIB were carried out in part in the Frederick Seitz Materials Research Laboratory Central Research Facilities, University of Illinois Urbana-Champaign.

Appendix

Calculation of ΔK^{change} Due to Crack Tip Transformation

Weight functions were introduced by Bueckner [56] and then expounded by Rice [57] to generate expressions for stress intensity factors due to an arbitrary traction distributions in cracked bodies. The source of the internal tractions can be the transformation strains enveloping the crack tips. The principle of the technique is that the weight functions can be derived if the analytical expressions for crack tip horizontal (u), vertical (v) displacement fields and the corresponding K values are known in the reference loading system. Then, the stress intensity solutions can be obtained for arbitrary loading direction. Transformation zone in the crack wake is demarcated with four different zones as shown in Fig. 11. The contribution from each zone to the change in stress intensity at the crack tip were calculated by employing weight functions. In the following we include the pertinent formulations for completeness which were discussed in detail in previous works [35, 36].

$$h_I(x, y, l) = \frac{H}{2K_I} \left(\frac{du^I(x, y, l)}{dl} \right) \quad (11)$$

So, the anisotropic weight functions h_x and h_y are defined as,

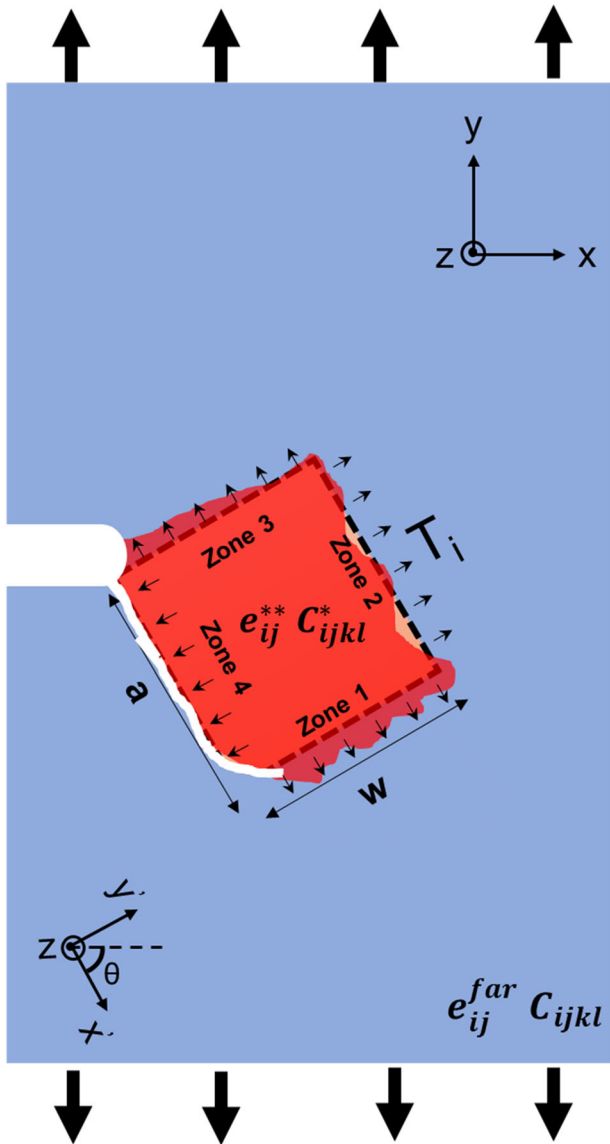


Fig. 11 Schematic illustrating the transformation region (in red) approximated as a rectangular zone with surface tractions on the zone perimeter. ΔK _transformation was calculated from each zone perimeter and combined to determine the effect of asymmetric transformation on stress intensity factor. The necessary values of the crack length (a), crack inclination (Θ) and zone height (w) were measured from optical micrographs at various crack lengths

$$h_{Ix'} = \frac{H}{2K_I} \left(\frac{du^I}{dl} \right) \tag{11a}$$

$$h_{Iy'} = \frac{H}{2K_I} \left(\frac{dv^I}{dl} \right) \tag{11b}$$

where K is the stress intensity factor and H is an elastic modulus term given by Sih [50]. Both mode I and mode II components are present and the weight functions in polar coordinates in the crack coordinate system ($x'y'z$) are defined as,

$$h_{Ix'} = \frac{H}{2K_I} \left(\frac{du^I}{d\theta} \frac{\sin \theta}{r} - \frac{du^I}{dr} \cos \theta \right) \tag{12a}$$

$$h_{Iy'} = \frac{H}{2K_I} \left(\frac{dv^I}{d\theta} \frac{\sin \theta}{r} - \frac{dv^I}{dr} \cos \theta \right) \tag{12b}$$

$$h_{IIx'} = \frac{H}{2K_{II}} \left(\frac{du^{II}}{d\theta} \frac{\sin \theta}{r} - \frac{du^{II}}{dr} \cos \theta \right) \tag{12c}$$

$$h_{IIy'} = \frac{H}{2K_{II}} \left(\frac{dv^{II}}{d\theta} \frac{\sin \theta}{r} - \frac{dv^{II}}{dr} \cos \theta \right) \tag{12d}$$

The crack tip displacement fields are analytically related to the mode I and II stress intensity factors by [50],

$$u^I = K_I \sqrt{2r} Re \left[\frac{1}{\mu_1 - \mu_2} \left(\mu_1 p_2 \sqrt{\cos \theta + \mu_2 \sin \theta} - \mu_2 p_1 \sqrt{\cos \theta + \mu_1 \sin \theta} \right) \right] \tag{13}$$

$$u^{II} = K_{II} \sqrt{2r} Re \left[\frac{1}{\mu_1 - \mu_2} \left(p_2 \sqrt{\cos \theta + \mu_2 \sin \theta} - p_1 \sqrt{\cos \theta + \mu_1 \sin \theta} \right) \right] \tag{14}$$

$$v^I = K_I \sqrt{2r} Re \left[\frac{1}{\mu_1 - \mu_2} \left(\mu_1 q_2 \sqrt{\cos \theta + \mu_2 \sin \theta} - \mu_2 q_1 \sqrt{\cos \theta + \mu_1 \sin \theta} \right) \right] \tag{15}$$

$$v^{II} = K_{II} \sqrt{2r} Re \left[\frac{1}{\mu_1 - \mu_2} \left(q_2 \sqrt{\cos \theta + \mu_2 \sin \theta} - q_1 \sqrt{\cos \theta + \mu_1 \sin \theta} \right) \right] \tag{16}$$

where μ_1 and μ_2 are the complex roots of the characteristic equation given below,

$$a_{11} \mu^4 - 2a_{16} \mu^3 + (2a_{12} + a_{66}) \mu^2 - 2a_{26} \mu + a_{22} = 0 \tag{17}$$

where a_{11} , a_{16} etc. are the elastic constants for FeMnNiAl in the crack coordinate system. The roots of the above equation are always complex or purely imaginary and always appear in conjugate pairs, μ_1 , μ_2 and. Term p_j and q_j are given as,

$$p_j = a_{11} \mu_j^2 + a_{12} - a_{16} \mu_j \tag{18}$$

$$q_j = a_{12} \mu_j + \frac{a_{22}}{\mu_j} - a_{26} \tag{19}$$

Sih [50] et al. also gave the solution for mode I and mode II stress intensity factors arising from the tractions on the crack surface (zone 4).

$$K_I = -\frac{1}{\pi \sqrt{a_0}} \int_0^a T_y(x') \left[\sqrt{\frac{a+x}{a-x}} - \frac{1}{2\beta_0} \right] dx' \tag{20}$$

$$K_{II} = -\frac{1}{\pi \sqrt{a_0}} \int_0^a T_x(x') \left\{ \frac{1}{2} \frac{\alpha_0^2}{\beta_0^2} + \frac{1}{2\beta_0} \left[\frac{a_{12}}{a_{11}} + (\alpha_0^2 + \beta_0^2) \right] \right\} dx' \tag{21}$$

$$H = -\frac{1}{8} \left(\frac{\mu_1 - \mu_2}{\mu_2} \right) \left\{ \frac{i}{\alpha_0 \beta_0} \left[\frac{a_{12}}{a_{11}} + (\alpha_0^2 - \beta_0^2) \right] + 1 \right\} \tag{22}$$

Table 3 24 possible variants with habit plane normal {0.1678, 0.7451, 0.6455} and transformation shear (0.0356, 0.1579, 0.1730)

n1 = 0.7451, n2 = 0.6455, n3 = 0.1678, and m1 = 0.1578, m2 = 0.1730, m3 = 0.0356			
v1	(- n1 - n2 n3) [- m1 m2 - m3]	v13	(- n3 - n1 n2) [m3 - m1 - m2]
v2	(- n1 n2 n3) [- m1 - m2 - m3]	v14	(- n3 - n1 - n2) [m3 - m1 m2]
v3	(- n1 n3 - n2) [- m1 - m3 m2]	v15	(n2 - n1 - n3) [- m2 - m1 m3]
v4	(- n1 n3 n2) [- m1 - m3 - m2]	v16	(- n2 - n1 - n3) [m2 - m1 m3]
v5	(- n1 - n3 n2) [- m1 m3 - m2]	v17	(n3 n2 - n1) [- m3 - m2 - m1]
v6	(- n1 - n3 - n2) [- m1 m3 m2]	v18	(n3 - n2 - n1) [- m3 m2 - m1]
v7	(- n1 n2 - n3) [- m1 - m2 m3]	v19	(n2 n3 - n1) [- m2 - m3 - m1]
v8	(- n1 - n2 - n3) [- m1 m2 m3]	v20	(- n2 n3 - n1) [m2 - m3 - m1]
v9	(n2 - n1 n3) [- m2 - m1 - m3]	v21	(n2 - n3 - n1) [- m2 m3 - m1]
v10	(- n2 - n1 n3) [m2 - m1 - m3]	v22	(- n2 - n3 - n1) [m2 m3 - m1]
v11	(n3 - n1 - n2) [- m3 - m1 m2]	v23	(- n3 n2 - n1) [m3 - m2 - m1]
v12	(n3 - n1 - n2) [- m3 - m1 m2]	v24	(- n3 - n2 - n1) [m3 m2 - m1]

For the orthotropic case, the solutions of Eq. (17) come out to be, $\mu_1 = \alpha_0 + i\beta_0$, $\mu_2 = -\alpha_0 + i\beta_0$ and a is the crack length.

Habit Plane Variants

According to Bain deformation theory, for a BCC to FCC austenite to martensite transformation, there can be three correspondent martensite variants. The austenite martensite interface is comprised of an invariant plane commonly known as the habit plane. Further, to facilitate zero average distortion at the A/M interface, the corresponding martensite needs to be internally twinned according to phenomenological theory of martensitic transformation. This is the case in the current SMA in consideration as evidenced by the TEM image of the internally twinned martensite (Fig. 9b). As mentioned in the results “Stress–Strain Response at RT” section, the habit plane was calculated by employing the energy minimization theory [41, 42]. The lattice constants for the FeMnNiAl austenite and martensite used for the calculation were obtained from an earlier study [13]. For each Bain correspondence pair, there exists a stretch tensor for the BCC to FCC transformation. These stretch tensors are obtained using the lattice constants for BCC austenite and FCC martensite [43]. For each of these Bain correspondence pairs, a unique solution for the twin plane and twinning shear is obtained for the internally twinned martensite. With this solution, the habit plane normal and transformation shear direction can be obtained by invoking the kinematic compatibility between the martensite and austenite phase. The steps required to obtain this solution are detailed in these earlier studies [41, 76]. The three stretch tensors used for the transformation are given as,

$$U_1 = \text{diag}(\eta_2, \eta_1, \eta_1), U_2 = \text{diag}(\eta_1, \eta_2, \eta_1), \text{ and } U_3 = \text{diag}(\eta_1, \eta_1, \eta_2) \quad (23)$$

Here η_1 and η_2 are obtained from the lattice constants of BCC and FCC phases which are $a_{\text{BCC}} = 0.2903$ nm and $a_{\text{FCC}} = 0.3672$ nm,

$$\eta_1 = \frac{a_{\text{FCC}}}{\sqrt{2}a_{\text{BCC}}} \quad \eta_2 = \frac{c_{\text{FCC}}}{a_{\text{BCC}}} = \frac{a_{\text{FCC}}}{a_{\text{BCC}}} \quad (24)$$

The habit plane and transformation shear directions obtained for FeMnNiAl by using the stretch tensors is listed in Table 3.

References

- Mohd Jani J, Leary M, Subic A, Gibson MA (2014) A review of shape memory alloy research, applications and opportunities. *Mater Des* 56:1078–1113
- Duerig KNMTW, Stöckel D, Wayman CM (eds) (1990) Engineering aspects of shape memory alloys. Butterworth-Heinemann, Boston
- Otsuka K, Wayman CM (1999) Shape memory materials. Cambridge University Press, Cambridge
- Chowdhury P, Canadinc D, Sehitoglu H (2017) On deformation behavior of Fe-Mn based structural alloys. *Mater Sci Eng R* 122:1–28
- Sato A, Chishima E, Soma K, Mori T (1982) Shape memory effect in $\gamma \rightleftharpoons \epsilon$ transformation in Fe-30Mn–1Si alloy single crystals. *Acta Metall* 30(6):1177–1183
- Abuzaid W, Sehitoglu H (2018) Superelasticity and functional fatigue of single crystalline FeNiCoAlTi iron-based shape memory alloy. *Mater Des* 160:642–651
- Hornbogen E, Jost N (1991) Alloys of iron and reversibility of martensitic transformations. In: European symposium on martensitic transformation and shape memory properties, 16–18 Sept 1991, France, 1991, vol 1, pp. 199–210
- Maki T, Kobayashi K, Minato M, Tamura I (1984) Thermoelastic martensite in an ausaged Fe-Ni-Ti-Co alloy. *Scr Metall* 18(10):1105–1109

9. Sehitoglu H, Karaman I, Zhang XY, Chumlyakov Y, Maier HJ (2001) Deformation of FeNiCoTi shape memory single crystals. *Scr Mater* 44(5):779–784
10. Sehitoglu H, Zhang XY, Kotil T, Canadinc D, Chumlyakov Y, Maier HJ (2002) Shape memory behavior of FeNiCoTi single and polycrystals. *Metall Mater Trans A* 33(12):3661–3672
11. Sohmura T, Oshima R, Fujita FE (1980) Thermoelastic FCC-FCT martensitic transformation in Fe-Pd alloy. *Scr Metall* 14(8):855–856
12. Omori T et al (2011) Superelastic effect in polycrystalline ferrous alloys. *Science* 333(6038):68–71
13. Ojha A, Sehitoglu H (2016) Transformation stress modeling in new FeMnAlNi shape memory alloy. *Int J Plast* 86:93–111
14. Sehitoglu H, Efstathiou C, Maier HJ, Chumlyakov Y (2005) Magnetization, shape memory and hysteresis behavior of single and polycrystalline FeNiCoTi. *J Magnet Magnet Mater* 292:89–99
15. Tanaka Y, Himuro Y, Kainuma R, Sutou Y, Omori T, Ishida K (2010) Ferrous polycrystalline shape-memory alloy showing huge superelasticity. *Science* 327(5972):1488–1490
16. Omori T, Kainuma R (2017) Martensitic transformation and superelasticity in Fe–Mn–Al-based shape memory alloys. *Shape Mem Superelast* 3(4):322–334
17. Abuzaid W, Sehitoglu H (2019) Shape memory effect in FeMnNiAl iron-based shape memory alloy. *Scr Mater* 169:57–60
18. Abuzaid W et al (2019) FeMnNiAl iron-based shape memory alloy: promises and challenges. *Shape Mem Superelast*. <https://doi.org/10.1007/s40830-019-00230-9>
19. Vollmer M et al (2015) On the effect of gamma phase formation on the pseudoelastic performance of polycrystalline Fe–Mn–Al–Ni shape memory alloys. *Scr Mater* 108:23–26
20. Omori T, Okano M, Kainuma R (2013) Effect of grain size on superelasticity in Fe–Mn–Al–Ni shape memory alloy wire. *APL Mater* 1(3):032103
21. Ozcan H et al (2018) Microstructural design considerations in Fe–Mn–Al–Ni shape memory alloy wires: effects of natural aging. *Scr Mater* 142:153–157
22. Tseng L-W, Ma J, Vollmer M, Krooß P, Niendorf T, Karaman I (2016) Effect of grain size on the superelastic response of a FeMnAlNi polycrystalline shape memory alloy. *Scr Mater* 125:68–72
23. Omori T, Iwaizako H, Kainuma R (2016) Abnormal grain growth induced by cyclic heat treatment in Fe–Mn–Al–Ni superelastic alloy. *Mater Des* 101:263–269
24. Ma J, Hornbuckle B, Karaman I, Thompson G, Luo Z, Chumlyakov YI (2013) The effect of nanoprecipitates on the superelastic properties of FeNiCoAlTi shape memory alloy single crystals. *Acta Mater* 61(9):3445–3455
25. Cui J et al (2006) Combinatorial search of thermoelastic shape-memory alloys with extremely small hysteresis width. *Nat Mater* 5(4):286
26. Lei C, Li L, Shu Y, Li J (2010) Austenite–martensite interface in shape memory alloys. *Appl Phys Lett* 96(14):141910
27. Kajiwara S (1999) Characteristic features of shape memory effect and related transformation behavior in Fe-based alloys. *Mater Sci Eng A* 273:67–88
28. Alkan S, Chowdhury P, Sehitoglu H, Rateick RG, Maier HJ (2016) Role of nanotwins on fatigue crack growth resistance: experiments and theory. *Int J Fatigue* 84:28–39
29. Chowdhury P, Sehitoglu H (2016) Mechanisms of fatigue crack growth: a critical digest of theoretical developments. *Fatigue Fract Eng Mater Struct* 39(6):652–674
30. Chowdhury P, Sehitoglu H, Rateick R (2016) Recent advances in modeling fatigue cracks at microscale in the presence of high density coherent twin interfaces. *Curr Opin Solid State Mater Sci* 20(3):140–150
31. Melton K, Mercier O (1979) Fatigue of NiTi thermoelastic martensites. *Acta Metall* 27(1):137–144
32. McKelvey A, Ritchie R (2001) Fatigue-crack growth behavior in the superelastic and shape-memory alloy Nitinol. *Metall Mater Trans A* 32(3):731–743
33. Sgambitterra E, Maletta C, Furguele F, Sehitoglu H (2018) Fatigue crack propagation in [0 1 2] NiTi single crystal alloy. *Int J Fatigue* 112:9–20
34. Sgambitterra E, Maletta C, Magarò P, Renzo D, Furguele F, Sehitoglu H (2019) Effects of temperature on fatigue crack propagation in pseudoelastic NiTi shape memory alloys. *Shape Mem Superelast* 5(3):278–291
35. Wu Y, Ojha A, Patriarca L, Sehitoglu H (2015) Fatigue crack growth fundamentals in shape memory alloys. *Shape Mem Superelast* 1(1):18–40
36. Yaacoub J, Wu Y, Abuzaid W, Canadinc D, Sehitoglu H (2019) Martensite variant localization effects on fatigue crack growth: the CuZnAl example. *Scr Mater* 171:112–117
37. Robertson SW, Pelton AR, Ritchie RO (2012) Mechanical fatigue and fracture of Nitinol. *Int Mater Rev* 57(1):1–37
38. Wu Y, Yaacoub J, Brenne F, Abuzaid W, Canadinc D, Sehitoglu H (2019) Deshielding effects on fatigue crack growth in shape memory alloys: a study on CuZnAl single-crystalline materials. *Acta Mater* 176:155–166
39. Efstathiou C, Sehitoglu H (2008) Local transformation strain measurements in precipitated NiTi single crystals. *Scr Mater* 59(12):1263–1266
40. Carroll J et al (2009) Investigation of fatigue crack closure using multiscale image correlation experiments. *Eng Fract Mech* 76(15):2384–2398
41. Zhang X, Sehitoglu H (2004) Crystallography of the B2 → R → B19' phase transformations in NiTi. *Mater Sci Eng A* 374(1–2):292–302
42. Ball JM, James RD (1989) Fine phase mixtures as minimizers of energy. *Analysis and continuum mechanics*. Springer, New York, pp 647–686
43. Bhattacharya K (2003) Microstructure of martensite: why it forms and how it gives rise to the shape-memory effect. Oxford University Press, Oxford
44. Alkan S, Sehitoglu H (2019) Prediction of transformation stresses in NiTi shape memory alloy. *Acta Mater* 175:182–195
45. Huang B, Duan Y-H, Hu W-C, Sun Y, Chen S (2015) Structural, anisotropic elastic and thermal properties of MB (M = Ti, Zr and Hf) monoborides. *Ceram Int* 41(5):6831–6843
46. Zhang J-M, Zhang Y, Xu K-W, Ji V (2007) Young's modulus surface and Poisson's ratio curve for cubic metals. *J Phys Chem Solids* 68(4):503–510
47. Wagner M-X, Windl W (2008) Lattice stability, elastic constants and macroscopic moduli of NiTi martensites from first principles. *Acta Mater* 56(20):6232–6245
48. Verlinden B, Suzuki T, Delaey L, Guenin G (1984) Third order elastic constants of β -Cu-Zn-Al as a function of the temperature. *Scr Metall* 18(9):975–979
49. Tada H, Paris P, Irwin G (2000) The analysis of cracks handbook. ASME Press, New York
50. Sih GC, Paris P, Irwin GR (1965) On cracks in rectilinearly anisotropic bodies. *Int J FractMech* 1(3):189–203
51. Pataky GJ, Sangid MD, Sehitoglu H, Hamilton RF, Maier HJ, Sofronis P (2012) Full field measurements of anisotropic stress intensity factor ranges in fatigue. *Eng Fract Mech* 94:13–28
52. McMeeking R, Evans A (1982) Mechanics of transformation-toughening in brittle materials. *J Am Ceram Soc* 65(5):242–246
53. Evans A, Heuer A (1980) Transformation toughening in ceramics: Martensitic transformations in crack-tip stress fields. *J Am Ceram Soc* 63(5–6):241–248

54. Eshelby JD (1959) The elastic field outside an ellipsoidal inclusion. *Proc R Soc Lond Ser A* 252(1271):561–569
55. Mura T (2013) *Micromechanics of defects in solids*. Springer, New York
56. Bueckner H (1970) Novel principle for the computation of stress intensity factors. *Zeitsch Angew Mat Mech* 50(9):50
57. Rice JR (1972) Some remarks on elastic crack-tip stress fields. *Int J Solids Struct* 8(6):751–758
58. Kajiwara S, Kikuchi T (1990) Shape memory effect and related transformation behavior in Fe-Ni-C alloys. *Acta Metall Mater* 38(5):847–855
59. Alkan S, Sehitoglu H (2017) Non-Schmid response of Fe3Al: The twin-antitwin slip asymmetry and non-glide shear stress effects. *Acta Mater* 125:550–566
60. Patra A, Zhu T, McDowell DL (2014) Constitutive equations for modeling non-Schmid effects in single crystal bcc-Fe at low and ambient temperatures. *Int J Plast* 59:1–14
61. Alkan S, Wu Y, Sehitoglu H (2017) Giant non-Schmid effect in NiTi. *Extr Mech Lett* 15:38–43
62. Alkan S, Ojha A, Sehitoglu H (2018) The complexity of non-Schmid behavior in the CuZnAl shape memory alloy. *J Mech Phys Solids* 114:238–257
63. Hornbogen E (2004) Review thermo-mechanical fatigue of shape memory alloys. *J Mater Sci* 39(2):385–399
64. Van Humbeeck J (1991) Cycling effects, fatigue and degradation of shape memory alloys. *Le J Phys IV* 1(C4):189–197
65. Kohlhoff S, Gumbsch P, Fischmeister H (1991) Crack propagation in bcc crystals studied with a combined finite-element and atomistic model. *Philos Mag A* 64(4):851–878
66. Riedle J, Gumbsch P, Fischmeister HF (1996) Cleavage anisotropy in tungsten single crystals. *Phys Rev Lett* 76(19):3594
67. Mei Z, Morris J (1990) Influence of deformation-induced martensite on fatigue crack propagation in 304-type steels. *Metall Trans A* 21(12):3137–3152
68. Ritchie RO (1979) Near-threshold fatigue-crack propagation in steels. *Int Met Rev* 24(1):205–230
69. Beevers C, Cooke R, Knott J, Ritchie R (1975) Some considerations of the influence of sub-critical cleavage growth during fatigue-crack propagation in steels. *Metal Sci* 9(1):119–126
70. Barsom JM (1971) Fatigue-crack propagation in steels of various yield strengths. *J Eng Ind* 93(4):1190–1196
71. Hamilton RF, Sehitoglu H, Chumlyakov Y, Maier H (2004) Stress dependence of the hysteresis in single crystal NiTi alloys. *Acta Mater* 52(11):3383–3402
72. Sehitoglu H, Hamilton R, Maier H, Chumlyakov Y (2004) Hysteresis in NiTi alloys. *J Phys IV* 115:3–10
73. Bhattacharya K, Conti S, Zanzotto G, Zimmer J (2004) Crystal symmetry and the reversibility of martensitic transformations. *Nature* 428(6978):55
74. Gao Y, Casalena L, Bowers M, Noebe R, Mills M, Wang Y (2017) An origin of functional fatigue of shape memory alloys. *Acta Mater* 126:389–400
75. Mohammed ASK, Sehitoglu H (2020) Martensitic twin boundary migration as a source of irreversible slip in shape memory alloys. *Acta Mater* 186:50–67
76. Sehitoglu H et al (2000) Compressive response of NiTi single crystals. *Acta Mater* 48(13):3311–3326

Publisher's Note Springer Nature remains neutral with regard to jurisdictional claims in published maps and institutional affiliations.